ACS APPLIED MATERIALS & INTERFACES

Research Article

www.acsami.org

Microtube Bundle Carbon Derived from Paulownia Sawdust for Hybrid Supercapacitor Electrodes

Xiangrong Liu,[†] Mingtao Zheng,[‡] Yong Xiao,[‡] Yunhua Yang,[†] Lufeng Yang,[†] Yingliang Liu,*[,‡] Bingfu Lei,[‡] Hanwu Dong,[‡] Haoran Zhang,[‡] and Honggang Fu[§]

[†]Department of Chemistry, Jinan University, Guangzhou 510632, P.R. China

[‡]College of Science, South China Agricultural University, Guangzhou 510642, China

[§]School of Chemistry and Materias Science, Heilongjiang University, Harbin 150080, China

ABSTRACT: The structure and capacitive properties of microtube bundle carbons (MTBCs) from carbonization of paulownia sawdust (PS) followed by NaOH activation were investigated. Morphology analyses indicated that MTBCs had abundant micropores and mesopores with a high specific surface area of about 1900 $m^2 g^{-1}$. Cyclic voltammetry, galvanostatic charge/discharge, and electrochemical impedance spectroscopy studies demonstrated the excellent charge storage, transfer capability, and low impedance of MTBCs. The specific capacitance of MTBCs-4 was as high as 227 F g^{-1} at 2 mV s^{-1}. Experimental results indicated that MTBCs provide smooth charge-transfer pathways for the ions in electrolytes and gateways to micropores and mesopores in the bulk. The hybrid supercapacitor model of MTBCs based on electrical double-layer capacitors and electrostatic capacitors was discussed and demonstrated. MTBCs are electrostatic capacitors at low frequency current, and may provide the pathways for easy accessibility of efficient charge transmission and high energy storage.

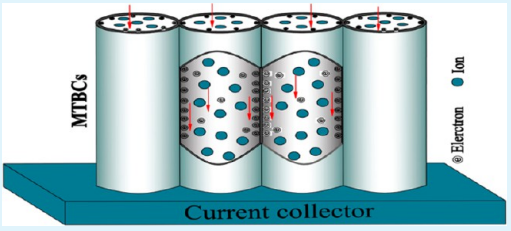

KEYWORDS: *paulownia sawdust, microtube bundle carbons, macropores, gateways, electrical double-layer capacitors, electrostatic capacitors*

1. INTRODUCTION

With the increase of fossil fuels depletion and environmental pollution, intensive research interests have been stimulated to develop the advanced devices for energy storage and management.[1,2] Among them, electrochemical double-layer capacitors, or supercapacitors, are widespread energy storage devices with high power density, fast charging, and long cycling life. In the device, the electrical energy is stored in an electrochemical double-layer capacitor formed at the interface between the charged surfaces of the electrode and electrolyte solution.[2,3] Currently, porous carbon materials are widely used as supercapacitor electrodes owing to their high surface area, lower cost, easy processing, nontoxicity, good electronic conductivity, well-developed pore-size distribution, and good physicochemical stability.[4] It has been demonstrated that the electrochemical performance greatly relies on its specific surface area, pore size distribution, pore shape and structure, electrical conductivity, and surface functionality.[4−6] For pore size and structure of materials, to obtain an ideal electrode, charge transportation pathways are necessary through the mesopores which could channel ions to abundant micropores in the electrolyte throughout the surface of the mesoporous channels.[4−6,13] However, the researchers paid little attention to the influence of the electrochemical properties by the shape and structure of macropores.

As a practical matter, supercapacitors with practical applications should exhibit excellent properties such as long cycle life, high capacitance, high power density, low impedance, as well as low cost.[6,7] A typical activated carbon material, with a specific surface area in the range 1000−2000 $m^2 g^{-1}$, exhibited gravimetric capacitances between 100 and 120 F g^{-1} in organic electrolytes, which suggested the low electron and ion conductivity and high impedance.[6−9] Although graphene, carbon nanotubes, and carbon fibers showed high gravimetric capacitances from 200 to 350 F g^{-1}, their high cost is a current big challenge for their commercialization as supercapacitors.[7,10−13] Fortunately, compared with artificial templates and precursors, many natural materials are generally abundant, renewable, inexpensive, and environmentally benign.[14,15] Thus, the utilization of natural biological components to construct carbon materials has received extensive attention.[14,15] For example, porous carbon materials have been prepared from cheap biomass residues and wastes, such as rice hull,[16] banana peel,[17] argan seed shells,[18] and so on. Paulownia wood, a common and abundant forestal waste biomass, contains an abundant porous structure of biopolymers in plant cell walls, such as celluloses, hemicelluloses, lignins, and proteins.[19]

Herein, we reported the preparation of microtube bundle carbons (MTBCs) from NaOH activation of the carbonized products of paulownia sawdust (PS). Owing to the high specific

Received: November 18, 2012
Accepted: May 20, 2013
Published: May 20, 2013

surface area and exceptional capacitor property caused by the macropore shape and structure, the PS-derived MTBCs were employed as hybrid supercapacitor electrode materials. As the galvanostatic charge/discharge and electrochemical impedance spectroscopy performance of MTBCs was different from that of typical porous carbons, a model of a MTBC supercapacitor based on electrical double-layer capacitors and electrostatic capacitors was also proposed. The electrostatic capacitors effect is generated at low frequency current based on the microtube bundle structure carbons. MTBCs provide smooth charge-transfer pathways for the ions in electrolytes and gateways to micropores and mesopores in the bulk. Furthermore, the novel model of MTBC supercapacitors has provided a potential way for developing the high power density and low impedance supercapacitor devices.

2. EXPERIMENTAL SECTION

2.1. Sample Preparation. In our experiments, all chemical reagents were analytical grade and used as received without further purification. Sodium hydroxide was purchased from Damao Chemical Reagent Company of Tianjin. The PS was obtained at a forest in Hunan province, China.

The schematic preparation of MTBCs was shown in Figure 1. PS was put in a tube furnace under N_2 flow and carbonized at 700 °C for

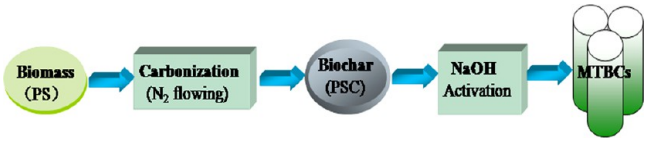

Figure 1. Schematic preparation of microtube bundle carbons (MTBCs).

2 h. Next, the paulownia sawdust carbon (PSC) was mixed with sodium hydroxide in a weight ratio of 2, 3, and 4 (sodium hydroxide/PSC), respectively. These mixture samples were heated up to 800 °C at a heating rate of 4 °C/min and then kept at this temperature for an additional 2 h. Afterward, the activated products were successively washed with distilled water until the pH came near 7, dried at 60 °C for 12 h, and ground, furnishing the MTBCs with uniform dimensions. These samples were marked as MTBCs-2, MTBCs-3, and MTBCs-4, in which the number represented the weight ratio of sodium hydroxide/MTBCs.

2.2. Characterization of MTBCs. Powder X-ray diffraction (XRD) patterns were recorded on a Bruker D8 X-ray diffractometer (Cu Kα, 40 kV, 20 mA, λ = 1.54056 Å). The morphologies were examined by scanning electron microscope (SEM, Philips SEM-XL30S). The element analyses of the carbonized and activated samples were determined on a Series II CHNS/O Analyzer 2400. Raman spectra were conducted on a LabRAM HR800 Raman spectrometer (Jobin-Yvon, HORIBA Group, France) with 532 nm wavelength incident laser light.

The N_2 adsorption−desorption isotherms of the samples were measured at 77 K using a 3H-2000PS2 Analyzer for determining their specific surface area. The specific surface area was calculated from the Brunauer−Emmett−Teller (BET) plot of the nitrogen adsorption isotherm. In addition, the pore size distribution of the samples was calculated from absorption branch isotherms by the Barrett−Joyner−Halenda (BJH) method.[20]

2.3. Electrochemical Measurements. Supercapacitor assembling and electrochemical testing were performed at a three-electrode system according to the literature.[10,14−17,21] The typical electrochemical experiments were conducted on a Iviumstat electrochemical workstation (Netherlands) in the three-electrode cell with 6.0 M KOH as electrolyte solution at room temperature. The test electrode was prepared by loading a slurry consisting of 75 wt % active material, 15 wt % carbon black, and 10 wt % poly(vinylidene fluoride) (in *N*-methylpyrrolidone) on a nickel foam, and dried at 80 °C for 1.5 h. Then, the electrodes were pressed at a pressure of 10 MPa and further dried at 100 °C for 12 h. The sample was used as a test electrode, platinum foil as a counter electrode, and Hg/HgO electrode as a reference electrode. Cyclic voltammetry curves were obtained in the potential range of −1.0 to 0 V vs Hg/HgO by varying the scan rate from 2 to 100 mV s^{-1}. Cycle stability was evaluated by performing galvanostatic cycling between −1.0 and 0 V at a scan rate of 20 mV s^{-1} for 1000 times. Charge−discharge measurements were conducted galvanostatically at 0.2−2.0 A g^{-1} over a voltage range of −0.9 to 0.1 V vs Hg/HgO. Electrochemical impedance spectroscopy was measured at the open circuit voltage in the frequency range from 0.005 Hz to 1 MHz with an alternate current amplitude of 5 mV.

3. RESULTS AND DISCUSSION

Chemical activation has been extensively employed in preparing porous activated carbons.[22] Normally, the carbon materials activated by KOH have a higher specific surface area than those activated by NaOH, because of the higher chemical activity of KOH.[23] However, when PSC was activated with KOH, the structure of the MTBCs was completely destroyed and porous activated carbons were obtained. Thus, activated carbons,[23] carbon nanospheres,[24] and carbon nanofibers[25] had been activated with NaOH to improve the porosity and enhance the supercapacitor performance. NaOH was employed to activate PSC to obtain MTBCs with excellent supercapacitor performance. The activation of carbon with NaOH was suggested as $6NaOH + C \rightarrow 2Na + 3H_2 + 2Na_2CO_3$, followed by the decomposition of Na_2CO_3 and/or reaction of Na_2CO_3/CO_2 with carbon.[22,23,25]

3.1. Characterization of Materials. Figure 2a shows the typical XRD patterns of the as-prepared PSC and MTBC samples. From the peaks at 2θ = 21.99 and 43.56°, it was clear that the samples contained disordered or amorphous carbons. Comparing the (002) and (100) peaks of MTBCs-2, those in MTBCs-4 had a markedly reduced intensity and were dramatically broadened. The full width at half-maximum of the (100) peak was ∼3°, indicating that the average in-plane crystal size was ∼5 nm by the Scherrer equation.[25] With increasing the usage of NaOH, the intensities of the peaks at (002) and (100) in MTBCs-3 and MTBCs-4 were decreased, while the full width at half-maximun increased. The intensities of MTBCs-2, MTBCs-3, and MTBCs-4 increased in a low-angle scatter versus PSC, which was in agreement with the high pore density. The XRD results revealed that the MTBCs contained poorly organized graphitic structures.

As shown in Figure 2d−f, the microtube bundle morphology of MTBCs could be obviously observed. In contrast with commercial activated carbons (b) and PSC (c), the microtube diameter was ∼30 μm and plenty of MTBC fragments were filled in the microtubes. The microtube bundle structure of MTBCs-3 was slightly damaged in comparison with MTBCs-2. However, the microtube bundle structure of MTBCs-4 was grievously destructed, and porous activated carbons could be obtained. These results indicate that the microtube bundle structure of MTBCs was damaged more seriously with the increasing usage of NaOH.

The elemental analysis results of the samples were listed in Table 1. The carbon content of PS is about 51%, and after carbonized, that of PSC increases to 85%. With increasing the usage of NaOH, the carbon content of the samples increased. On the contrary, the nitrogen and hydrogen contents of the MTBCs decreased. As shown in Table 1, the carbon, hydrogen,

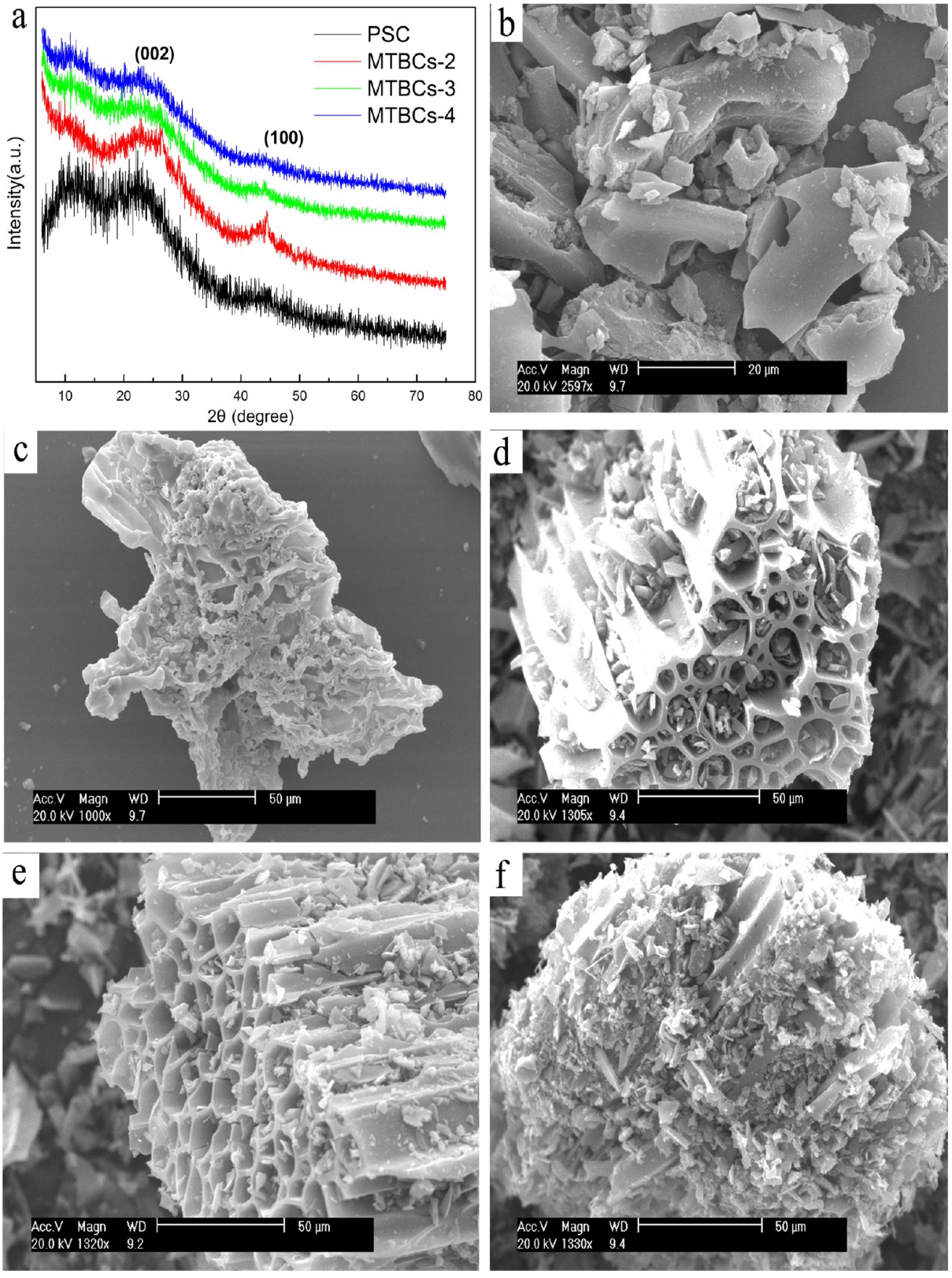

Figure 2. XRD patterns of samples (a). SEM images of the commercial ACs (b), PSC (c), MTBCs-2 (d), MTBCs-3 (e), and MTBCs-4 (f).

and nitrogen contents of MTBCs-4 were 94.32, 0.15, and 0.05%, respectively.

The specific surface area and pore size characterization of the MTBC samples were performed by combining high-resolution nitrogen (77.4 K) and argon (87.3 K) adsorption/desorption experiments with advanced methods based on density functional theory.[26] The porous characters of these materials were summarized in Table 1. It suggests that the specific surface area increases from 380 to 1962 $m^2 g^{-1}$ after the activation reaction, and the total pore volume of PSC is much less than that of

dx.doi.org/10.1021/am4012808 | ACS Appl. Mater. Interfaces 2013, 5, 4667−4677

Table 1. The Carbon, Hydrogen, and Nitrogen Content and Pore Structure Parameters of the MTBC Samples

sample	C (wt %)	H (wt %)	N (wt %)	S_{BET} [a] (m^2 g^{-1})	V_t [b] (cm^3 g^{-1})	V_{micro} [c] (cm^3 g^{-1})	V_{meso} [d] (cm^3 g^{-1})	D [e] (nm)
PS	51.49	6.55	0.19					
PSC	85.26	1.37	0.15	380	0.13	0.11	0.02	2.59
MTBCs-2	91.45	0.79	0.12	1842	0.91	0.40	0.51	2.01
MTBCs-3	92.68	0.48	0.08	1861	0.93	0.41	0.52	1.98
MTBCs-4	94.32	0.15	0.05	1962	0.94	0.40	0.54	1.91

[a]The specific surface area (S_{BET}) is calculated by the Brunauer–Emmett–Teller (BET) method. [b]V_t denotes the total pore volume. [c]V_{micro} represents the micropore volume. [d]V_{meso} stands for the Barrett mesopore and micropore volume obtained by subtracting V_{micro} from V_t. [e]D stands for the absorption average pore width (by BET).

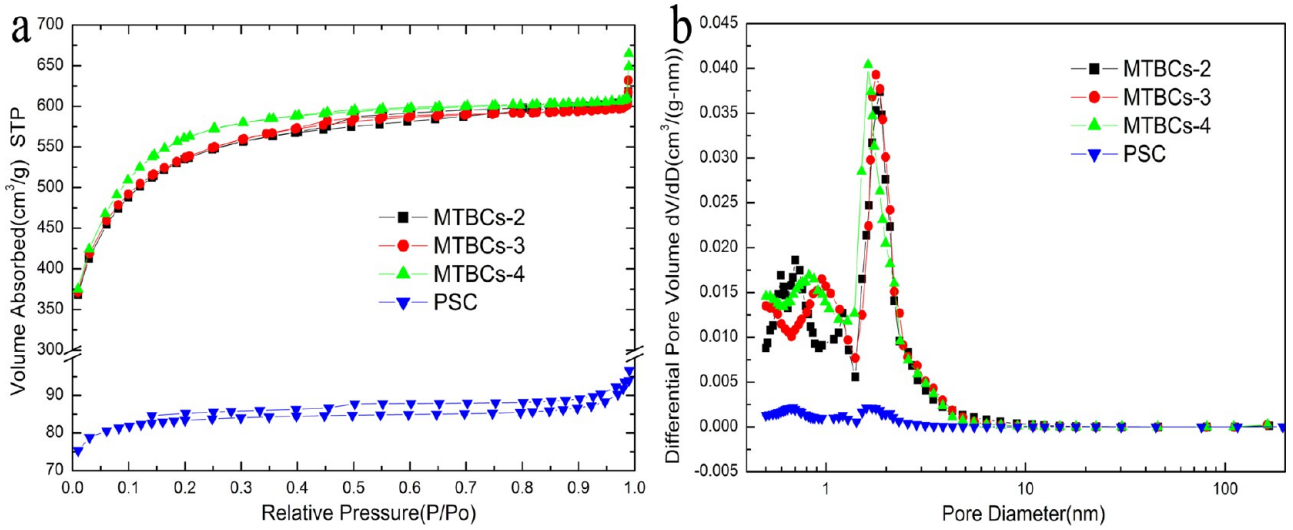

Figure 3. N_2 adsorption/desorption isotherms of MTBC samples and PSC (a). Pore size distribution of MTBC samples and PSC (b).

MTBCs. With the weight ratio of NaOH/PSC increased, the specific surface area and pore volume of the samples increased. MTBCs-4 had the highest specific surface area (1962 m^2 g^{-1}) and mesoporous ratio (57.45%) in the total pore volume than others. The similar average pore width of MTBCs was about 3 nm. The dominantly mesoporous structure and appropriately porous size were an advantage of ion diffusion and mass transfer of aqueous capacitors, consequently leading to a higher capacitance.[8] Therefore, the MTBCs could be an excellent electrode material in electrical double-layer capacitor application.

In Figure 3a, the N_2 adsorption–desorption isotherms of the samples were shown. For the PSC, it shows a type II shape (in the IUPAC classification) with a small hysteresis loop extending from P/P_0 = 0.20 to 0.99.[25] After activation reaction, MTBCs-2, MTBCs-3, and MTBCs-4 exhibit N_2 isotherms with steep uptakes below P/P_0 = 0.01 and a small hysteresis loop close to type IV, indicating the coexistence of micropores (<2 nm) and mesopores (2.50 nm) in these samples. Figure 3b presents the pore size distribution curves of the resulting PSC and MTBCs. The MTBC samples had sharp peaks at about 0.6, 0.8, and 2 nm, indicating the coexistence of hierarchical micropores, mesopores.[26] PSC contains relatively less micropores, mesopores, or macropores in comparison to MTBCs.

Although development of surfaces with small pores was inaccessible for ions which did not improve the capacitance performance, mesopores are less efficient than micropores that are larger than the ion size.[27,28] In comparison to the mesopore volume, an increased micropore volume more efficiently enhanced the specific capacitance of a carbon electrode in aqueous solutions.[13] For instance, highest surface areas and dominantly micropores with diameters larger than the ion size exhibit the best capacitive performance. Therefore, the correct combination of interconnected meso- and micropores and suitable pore size are the key for optimized capacitive performance.[13]

3.2. Electrochemical Properties of MTBC Samples. The specific capacitance can be estimated from the voltammetric charge surrounded by the cyclic voltammetry curves according to the following formula:[29,30]

$$C_s = \frac{Q}{\Delta V \times M} = \frac{1}{2\Delta V}\int_{V_i}^{V_f} \frac{|I|}{dV/dt}\,dV = \frac{\int_{V_i}^{V_f} |I|\,dV}{2 \times S \times \Delta V} \quad (1)$$

where C_s is the specific capacitance of the electrode based on the mass of active materials (F g^{-1}), Q is the sum of anodic and cathodic voltammetric charges on positive and negative scans (C), I is the sample current density (A g^{-1}), M is the weight of active materials (g), ΔV is the total potential deviation of the voltage window (V), and S is the scanning rate (V/s).

In order to evaluate the electrochemical performance of MTBCs, the energy density and power density of the MTBCs-3 and PSC were estimated, using the following equations:[11,12,30]

$$C_m = \frac{C}{M} = \frac{I\Delta t}{\Delta V \times M} \quad (2)$$

$$E = \frac{1}{2} \times C_m \times \Delta V^2 \quad (3)$$

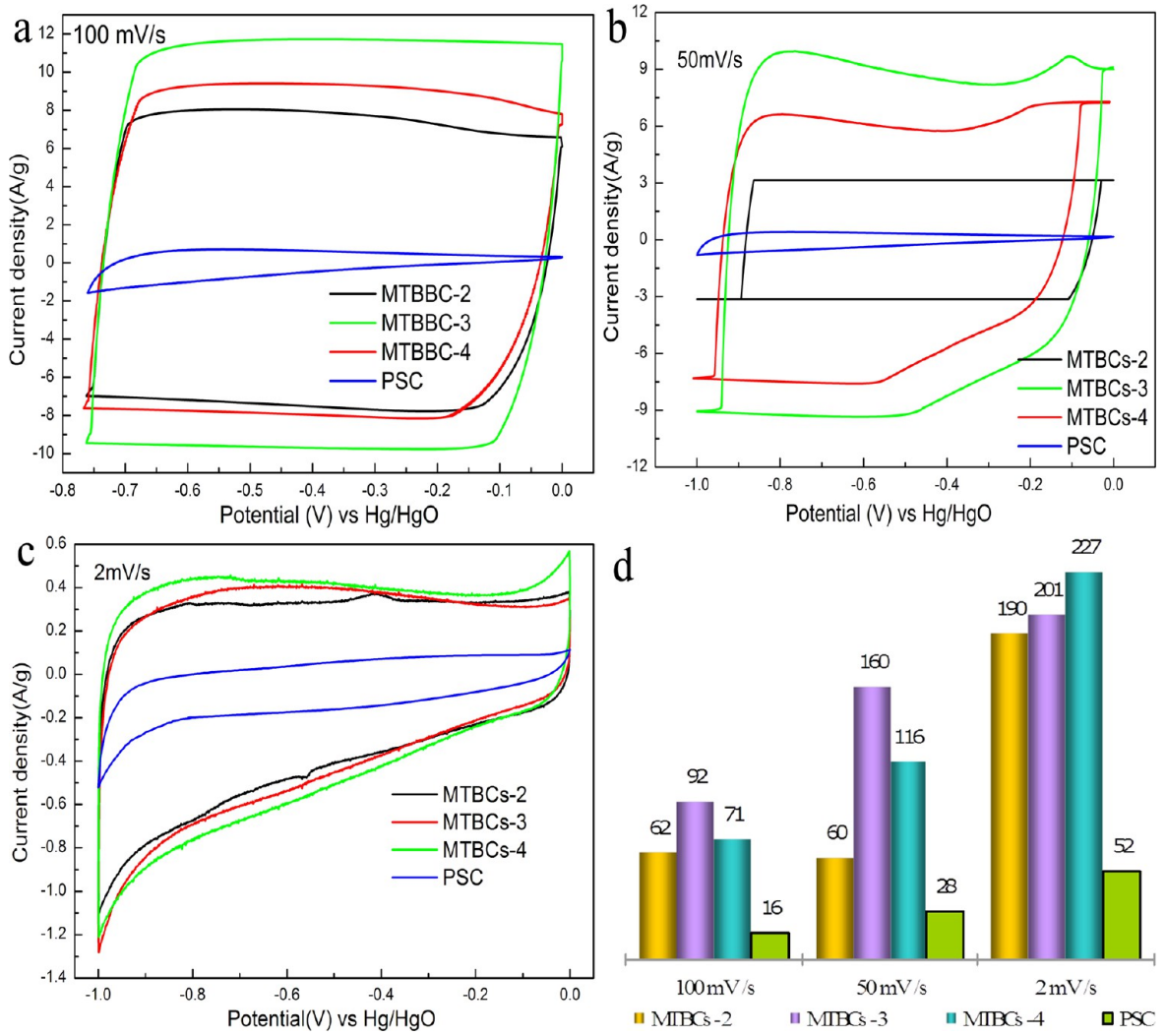

Figure 4. Cyclic voltammetry curves of MTBCs-2 (a), MTBCs-3 (b), and MTBCs-4 (c) in 6 mol·L^{-1} KOH at different scan rates and room temperature. The discharge specific capacitance of samples at different scan rates (d).

$$R_{ESR} = \frac{V_{drop}}{I_{cons}} \quad (4)$$

$$P_{max} = \frac{\Delta V^2}{4M \times R_{ESR}} \quad (5)$$

where C_m (F g^{-1}) is the measured device capacitance, I (A) is the discharge current, ΔV (V) represents the potential change within the discharge time Δt (s), M (g) is the total mass of the active material on the two electrodes, E (J g^{-1}) refers to the energy density, V_{drop} is the voltage drop at the beginning of the discharge under certain constant current I_{cons}, P_{max} (W g^{-1}) is the maximum power density, and R_{ESR} (Ω) is the equivalent series resistance (ESR) of the electrode.

For the convenience of comparison with the electrochemical performance of MTBC materials, the PSC as a porous carbon material was also to characterize the electrochemical performance by cyclic voltammetry and galvanostatic charge/discharge. The cyclic voltammetry curves at different potential scan rates were shown in Figure 4a–c. The remarkable difference in electrochemical property between the MTBC samples and PSC could be easily recognized. In detail, the PSC exhibited small rectangular curves corresponding to low capacitances due to low specific surface area, while the MTBC samples presented capacitive behavior with the roughly rectangular-like shapes and a few humps in these cyclic voltammetry curves. The cyclic voltammetry curves of the MTBC samples were the imaginary rectangular shape at a scan rate of 100 mV s^{-1}. The cyclic voltammetry curves of MTBC samples and PSC were the imaginary rectangular shape at a scan rate of 50 and 2 mV s^{-1} (Figure 4b,c).

The specific capacitance of the samples can be calculated according to formula 1. As shown in Figure 4d, the specific capacitances of MTBCs and PSC at different scan rates of 100, 50, and 2 mV s^{-1} were given. It can be observed that the specific capacitance of PSC was much lower than those of MTBC samples. With decreasing scan rate, all the specific capacitances of MTBCs were inversely increased. MTBCs-3 exhibited the highest capacitance at a scan rate of 100 mV s^{-1} (92 F g^{-1}) and 50 mV s^{-1} (160 F g^{-1}). However, at a scan rate of 2 mV s^{-1}, the MTBCs-4 showed the highest capacitance (about 227 F g^{-1}), although MTBCs-2 and MTBCs-3 also exhibited outstanding capacitances. Interestingly, MTBCs-3 showed the highest capacitance at 50 and 100 mV s^{-1}, and it was 100 F g^{-1} more than that of MTBCs-2; however, it was less than that of MTBCs-4 at 2 mV s^{-1}. This phenomenon was

dx.doi.org/10.1021/am4012808 | ACS Appl. Mater. Interfaces 2013, 5, 4667–4677

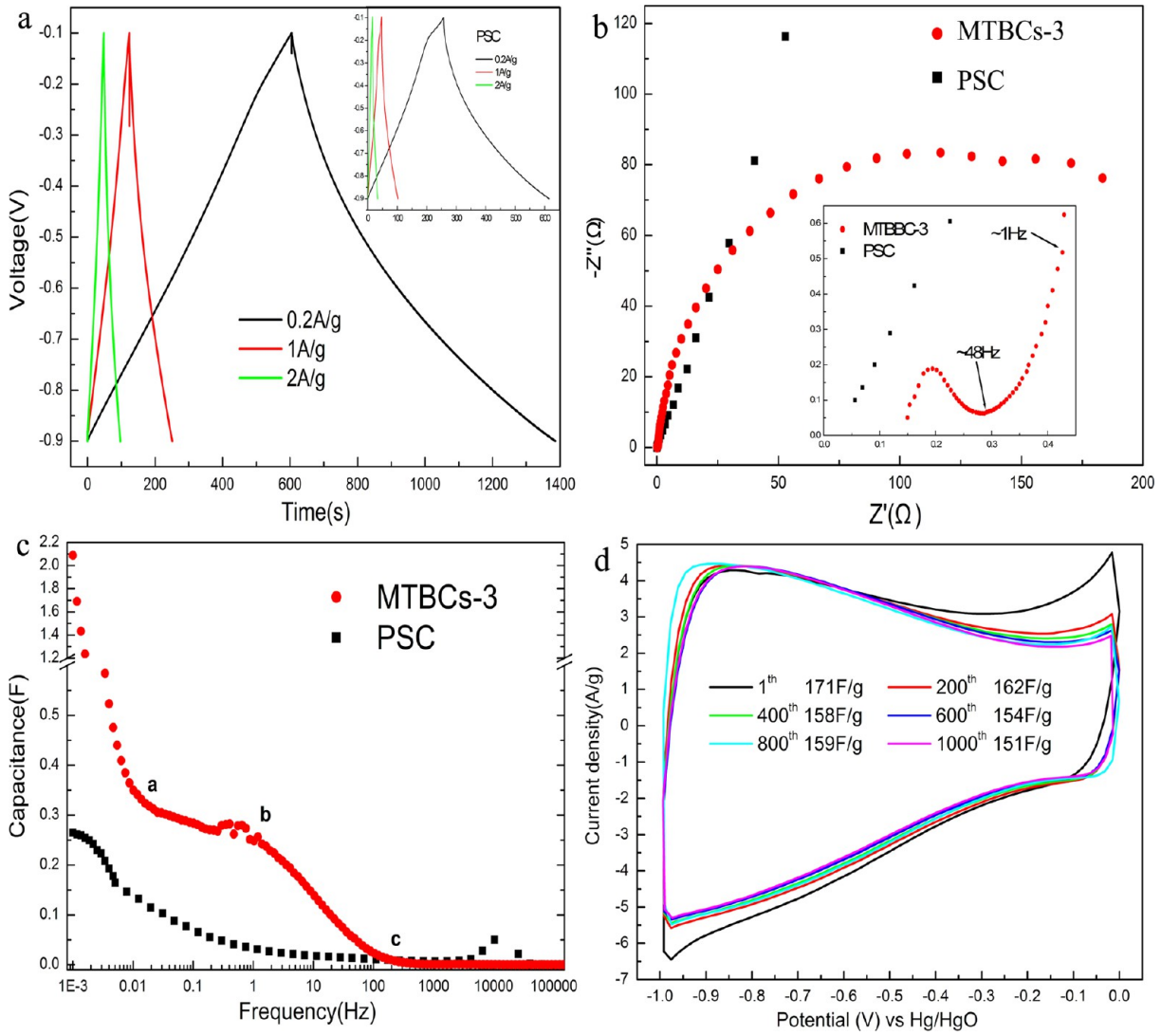

Figure 5. Galvanostatic charge/discharge curves of MTBCs-3 electrode at different constant current densities (inset: galvanostatic charge/discharge curves of PSC) (a). Nyquist plot for MTBCs-3 electrode (inset: magnified 0−0.4Ω region) (b). The Bode plot for MTBCs-3 electrode showing the frequency response of the gravimetric capacitance (c). Cyclic voltammetry curves and cycle life for MTBCs-3 measured at a scan rate of 20 mV s^{-1} (d).

different from that of typical porous carbons for which the specific capacitance performance was directly related to specific surface area and pore volume.[5,6]

It is well-known that the galvanostatic charge/discharge measurement was a more accurate technique for supercapacitors. As shown in the galvanostatic charge/discharge curves of MTBCs-3 (Figure 5a) and PSC (Figure 5a, inset), the discharge time of the MTBCs-3 was remarkably longer in comparison with PSC at both high and low current densities. It indicated that the MTBCs-3 offered a much larger capacitor, in good agreement with those obtained from cyclic voltammetry tests. For MTBCs-3, the discharge time was longer than the charge time at high current densities, while the charge time was longer than the discharge time at low current densities. In other words, the Coulombic efficiency (discharge/charge capacity) of MTBCs was higher at 1 A g^{-1} than that at 0.2 and 2 A g^{-1}. According to formula 2, the discharge capacitances of MTBCs-3 were 195, 158, and 123 A g^{-1} at current densities of 0.2, 1, and 2 A g^{-1}, respectively. In contrast, the much lower capacitances of PSC were 74, 51, and 37 F g^{-1}, respectively. In addition, the sharply decreased voltage drop at the beginning of the discharge could be recovered, which was different from that of porous carbon material.[5,6] We proposed that the interesting phenomenon resulted from an electrostatic field formed in a microtube bundle structure, in which electrons and ions were kept static to generate electrostatic capacitors at the beginning of discharge.

ESR was employed to further evaluate the impedance of materials. According to formula 4, we could obtain the ESR were 0.21, 0.18, and about 0.1Ω from the discharge curves of MTBCs-3 at a constant current of 0.2, 1, and 2 A g^{-1}, respectively. It suggested that the impedance of MTBCs-3 was much lower than that of PSC. According to formulas 3 and 5, the energy densities (E) were 17.3, 13.9, and 10.8 Wh/kg and the power densities (P) were 761, 888, and 1600 W/kg at currents of 0.2, 1, and 2 A g^{-1}, respectively.

In order to further investigate the performance of our samples, electrochemical impedance spectroscopy measurement was employed to collect the impedance character at the open-circuit potential by applying a small amplitude of

dx.doi.org/10.1021/am4012808 | ACS Appl. Mater. Interfaces 2013, 5, 4667−4677

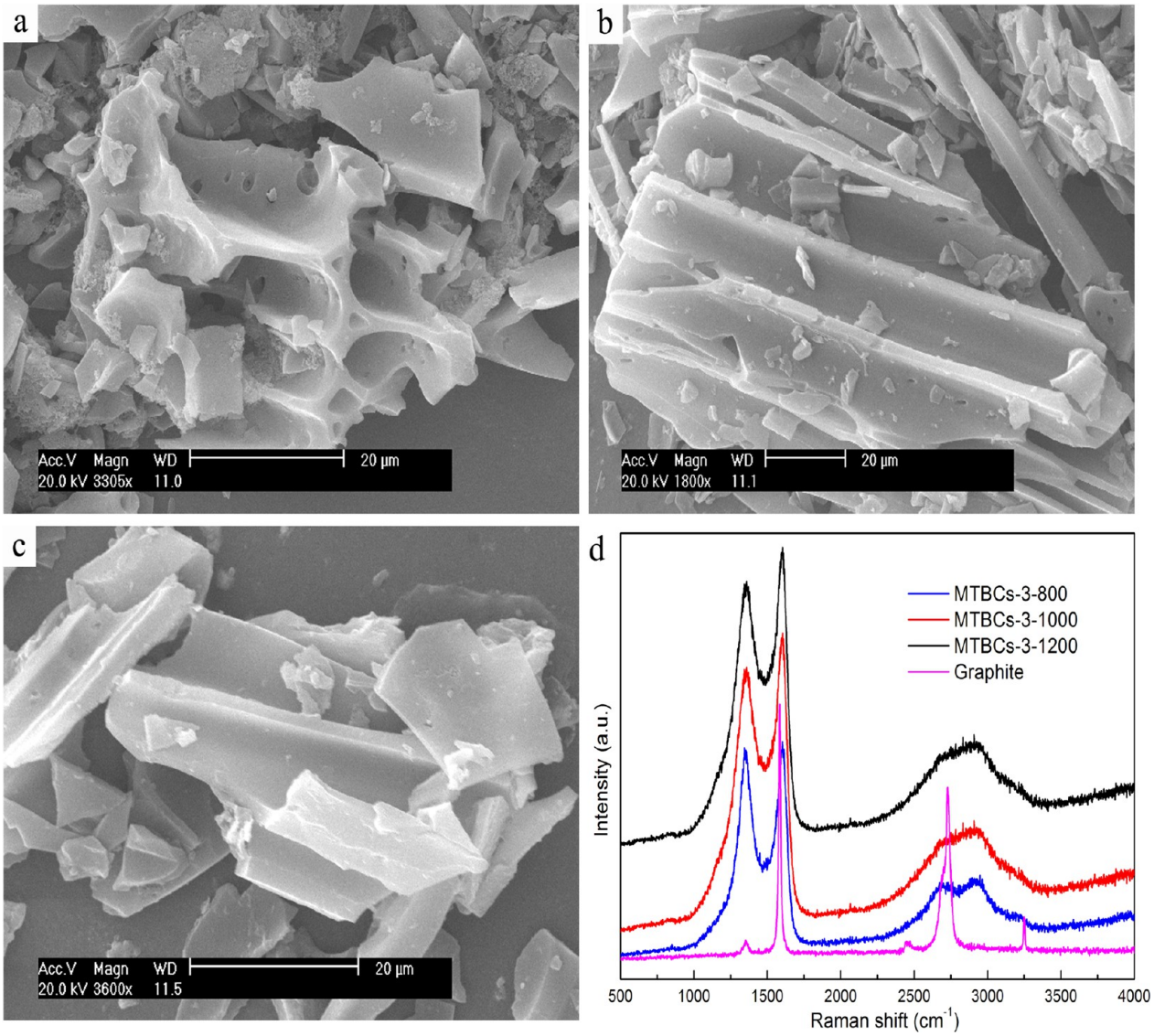

Figure 6. SEM images of MTBCs-3 after a 1000 cycle test process (a), SEM images of MTBCs-3 after different graphization temperatures: MTBCs-3-1000 (b); MTBCs-3-1200 (c). The Raman spectrum of MTBCs-3-800, MTBCs-3-1000, MTBCs-3-1200, and graphite (d).

alternative interrupting potential (e.g., ±10 mV) over a wide range of frequency f (e.g., 1 mHz to 1 MHz), by which the relationship between the imaginary part of impedance Z'' and frequency f was provided. The capacitance can be calculated by formula 6.[13] Using a linear portion of the C vs $\log f$ curve is called the Bode plot. The electrochemical impedance spectroscopy can also be expressed as a Nyquist diagram, where the imaginary part of impedance, $Z(f)''$, is plotted against the real part of impedance, $Z(f)'$.

$$C = \frac{-1}{2\pi f Z''} \tag{6}$$

A frequency response analysis of the frequency range from 1 MHz to 5 mHz yields the Nyquist plot, shown in Figure 5b. For PSC, the impedance plot showed almost linear behavior with a phase shift of 45°. This plot, a typical impedance plot of porous carbon material, accounted for double-layer charge-storage phenomena. In comparison, two semicircles of the MTBCs-3 plot can be observed in the complex plane because relaxation processes involve double-layer capacitance capacitors (C_{dl}) and electrostatic capacitors (C_P) coupled with ohmic elements.[13] For MTBCs-3, a transition state between the big quarter-circle and small semicircle was observed at a frequency of about 48 Hz in the high-frequency range (Figure 5b, inset) from the magnified data, corresponding to a resistance of 0.4Ω. The diffusion of electrolyte ions stopped at about 1 Hz, and thereafter, the whole of electrical double-layer capacitance was reached.[31] The smaller semicircle meant smaller charge transfer resistance. Besides, the sloped curves in the Nyquist impedance spectrum of the general electrode were obviously not observed.

In Figure 5c, the Bode plot showed that the MTBCs-3 and PSC were a pure resistance at the high frequency region, indicating that the electrolyte ions probably could not penetrate into micropores under high frequencies. In the high-to-medium frequency region (10^4–1 Hz), MTBCs-3 showed electrostatic capacitor transfer resistance associated with the porous structure of the electrodes. The capacitance increased at about 300 Hz and reached 0.3 F around 1 Hz (at point b in Figure 5c). At low frequency ranges (less than 1 Hz), in comparison with PSC, the Bode plot of MTBCs-3 sharply increased when the frequency was less than 0.03 Hz (at point a in Figure 5c). As a result, electrostatic capacitors may be

dx.doi.org/10.1021/am4012808 | ACS Appl. Mater. Interfaces 2013, 5, 4667–4677

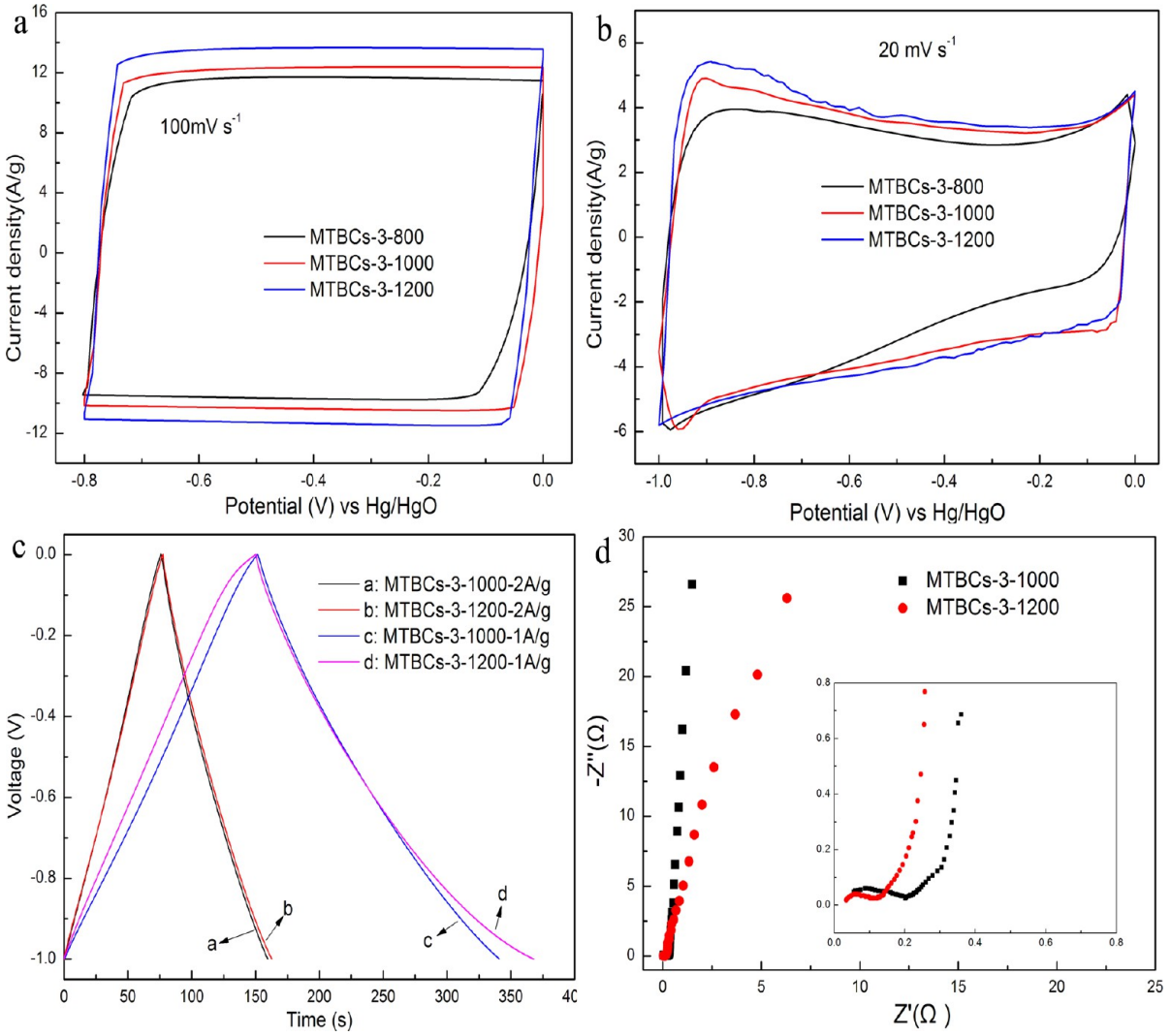

Figure 7. Cyclic voltammetry curves of MTBCs-3-800, MTBCs-3-1000, and MTBCs-3-1200 in 6 mol·L^{-1} KOH at a scan rate of 100 mV s^{-1} (a) and 20 mV s^{-1} (b). Galvanostatic charge/discharge curves of MTBCs-3-1000 and MTBCs-3-1200 electrodes at different constant current densities (c). Nyquist plot for MTBCs-3 electrode (inset: magnified 0−0.8Ω region) (d).

formed at nearly direct current ranges based on microtube bundle structure.

From the above results, the Nyquist plot and Bode plot of MTBCs-3 were obviously different from typical porous carbon material. We studied the influence of the macropore shape and structure of MTBCs on the material electrochemical properties. We assumed that electrostatic capacitors were formed in carbon microtubes.[5,6,13] When both electrostatic capacitor and electrical double-layer capacitor contributions were considered, a different equivalent circuit had to be drawn (Figure 8a).[13] These two semicircles intersected the Z' axis at three points: Z' = R_S, R_S + R_F, and R_S + R_F + $R_{F'}$. The radii of the two semicircles were determined by the desorption resistance (R_F) and electrostatic capacitors resistance ($R_{F'}$).[13] The impedance response of this equivalent circuit was shown in Figure 8b. It was known that this curve was perfectly matched with the Nyquist plot of MTBCs-3.

Furthermore, the life cycle experiments were performed at a sweep rate of 20 mV s^{-1} for 1000 cycles by cyclic voltammetry in order to investigate the cycling stability of MTBCs. As shown in Figure 5d, cyclic voltammetry curves were given at the 1st, 200th, 400th, 600th, 800th, and 1000th cycles, respectively. The specific capacitance of MTBCs-3 was 171 F g^{-1} at the 1st cycle, 162 F g^{-1} at the 200th cycle, and 151 F g^{-1} at the 1000th cycle, which suggested that over 88% of the original specific capacitance remained for the MTBCs-3 electrode after 1000 cycles. However, more than 5.5% of the original specific capacitance was lost in the first 200 cycles, which was a large part of the total loss of specific capacitance. Figure 6a showed the morphology of MTBCs-3 after the 1000 cyclic voltammetry cycles test process. The SEM indicated that MTBCs-3 was electrochemically stable, in spite of the fact that the microtube bundle structure of the sample was destructed to some extent. This is consistent with the cyclic voltammetry stability results.

3.3. The Electrochemical Properties of MTBCs after Different Graphization Temperatures. From the above cyclic voltammetry results, the MTBCs had a low capacitance at a high potential scan rate. Thus, we did some graphization at different temperatures (800, 1000, and 1200 °C) for MTBCs-3 and marked them as MTBCs-3-800, MTBCs-3-1000, and MTBCs-3-1200, respectively. As shown in Figure 6b,c, the SEM morphology of MTBCs-3-1000 (b) and MTBCs-3-1200 (c) samples followed by graphization from MTBCs-3 could be

dx.doi.org/10.1021/am4012808 | ACS Appl. Mater. Interfaces 2013, 5, 4667−4677

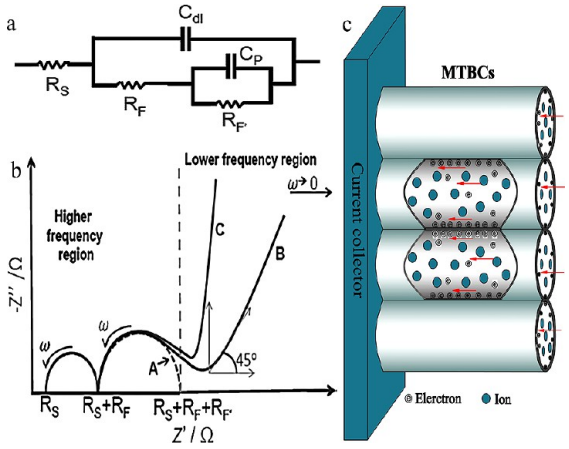

Figure 8. RC circuits for series and parallel connect resistor and capacitor, representing an equivalent circuit (simplest) of a capacitor. R = resistor, C = capacitor. Equivalent circuits considering both C_{dl} (in parallel to R_F) and C_P (in parallel to $R_{F'}$) in series with R_S are shown in part a.[13] The AC responses to the latter two circuits are shown in part b.[13] The schematic figure of the MTBC supercapacitor model is shown in part c.

observed. In contrast with MTBCs-3 (Figure 2c), the microtube bundle structure of MTBCs-3-1200 was seriously destroyed. In order to obtain the graphization degree, the Raman spectra were further conducted to the carbon bonds. As Figure 6d shows, the G band at 1585 cm^{-1} is ascribed to the vibration of sp^2-bonded carbon atoms in a two-dimensional hexagonal lattice and is associated with the E_{2g} mode of the graphite.[32] The peak at around 1350 cm^{-1} (D band) is related to the vibration of carbon atoms with dangling bonds in the termination plane of disordered graphite or glass carbon.[32] The intensity ratio (I_D/I_G) is employed to correlate the structural purity to the graphite.[32] Thus, the Raman spectrum (Figure 6d) reveals that the graphization degree of MTBCs-3-1200 is higher than MTBCs-3-800, but it is still not graphite. In this temperature range (lower than 2000 °C), the graphization is not necessarily related to the carbonization temperature.

In addition, the electrochemical capacitive behaviors of the MTBCs-3 treated at different temperatures were also necessary to examine. As can be seen in Figure 7, a higher specific capacitance can be obtained by simply increasing the treatment temperature from 800 to 1200 °C. The cyclic voltammetry curves of the MTBCs-3-1200 exhibited an ideal rectangular shape and higher specific capacitance (about 14 and 25 F g^{-1}) than MTBCs-3 at 100 and 20 mV s^{-1}, indicating that the graphization process could improve the electronic conductivity of materials. In Figure 7c, the relationship between the specific capacitance and the current density is observed according to the galvanostatic charge and discharge results collected at current densities of 2 and 1 A g^{-1}. In comparison with the MTBCs-3 (Figure 5a) samples, the MTBCs-3-1000 and MTBCs-3-1200 samples show a longer discharge time, indicating that the better reversible charge−discharge composites have more graphite carbons. These results are consistent with the cyclic voltammetry experiments. Moreover, in comparison with the MTBCs-3 (Figure 5b) samples, the Nyquist plots of MTBCs-3-1000 and MTBCs-3-1200 (Figure 7d) exhibit a better capacitive behavior and lower charge transfer resistance.

3.4. The Possible Model of MTBC Supercapacitors. The SEM images of the samples are shown in Figure 2, from which we can conclude that the samples contained both MTBCs and porous activated carbons. According to reports in the literature,[5,6] the electron and electrolyte ion conductivity of granular activated carbon were low because electrons are transmitted via activated carbon particles and ions are transmitted via void space. Hence, the particle activated carbon electrode had a large internal resistance, because of the many contacting points between the insulating binder material and the particles.[5,6] Nevertheless, the carbon nanotube array enhanced the electronic and ionic conductivity significantly and had a lower resistance.[6,31] The electrolyte in macropores and its physicochemical properties were similar to those of the bulk electrolyte with the lowest resistance.[31]

On the basis of the results from both our experiments and others reported in the literature,[6,31−34] a model of MTBC supercapacitors was proposed, as shown in Figure 8c. This geometry had several advantages. First, the MTBCs were connected directly to the current collector by electron "superhighways"; consequently, this superior conducting network significantly enhanced the electronic conductivity of the composite. MTBCs are important for providing a smooth charge-transfer pathway for the ions in electrolytes. Macropores provide gateways to micropores and mesopores in the bulk. On the other hand, the micropore and mesopore size greatly enhanced the ionic conductivity of the MTBC/KOH composite. Ion buffering reservoirs could be formed in macropores between microtubes, and thus, the diffusion distances to the interior surfaces of liquid phase were minimized.[2,31] This deduction could explain why MTBCs-3 had a higher specific capacitance at a higher scan rate (100, 50 mV/s), as shown in Figure 4a and b.

Second, the tubular structure and high specific surface area reduced the diffusion length of ions in the carbon tube during the charge−discharge process, and thus ensured a high utilization of electrode materials, resulting in a high specific capacity.[35] The tubular wall served as the carrier which enhanced the rate and efficiency of electron and ion transmission. Thus, as shown in Figure 5a, the charge process was faster than discharge. For the microtube carbon, the charge process is like the water flow in a pipe. Electron and ion conductivity in the microtube carbon could be regarded as water flow in a round pipe of diameter (d) at a depth (h) of $0 \leq h \leq d$ (fullness degree: h/d, equal to electron and ion density). According to the open-channel flow theory of fluid mechanics, the maximum flow rate, Q_{max}, does not occur when the pipe is full, $Q_{full} = 0.929Q_{max}$; instead, it occurs when $h = 0.929d$.[36] This conclusion could explain why the Coulombic efficiency was obviously higher at high current densities, such as 1 A g^{-1} (Figure 5a).

Third, a microtube structure carbon was a small electrostatic capacitor, when the microtube carbons were charged at direct currents. At low frequency current, the countless electrons were gathered and transmitted at the microtube wall and electrolyte decomposition happened in the internal tube, as shown in Figure 8c. In other words, the microtube bundle carbon was a group of electrostatic capacitors at low frequency current, resulting in a sharp increase of capacitance of MTBCs-3 when the frequency was less than 0.02 Hz in the Bode plot, as shown in Figure 5c.

In the Poisson−Boltzmann equations of Gouy[37] and Chapman,[38] to evaluate the theoretical capacitances of MTBCs, the ions were modeled as point charges (apart from a possible nonzero distance of closest approach to the

electrode). According to the Poisson−Boltzmann theory, the capacitance of the MTBCs was written in the following form:

$$\frac{1}{C} = \frac{1}{C_\delta^1 + \cdots + C_\delta^i + \cdots + C_\delta^n} + \frac{1}{C_{\text{diff}}^1 + \cdots + C_{\text{diff}}^i + \cdots C_{\text{diff}}^n} \approx \frac{1}{n \cdot C_\delta^i} + \frac{1}{n \cdot C_{\text{diff}}^i}$$

where C_δ^i and C_{diff}^i are the capacitances of microtube carbon number "i" (the total number of carbon microtubes is n) at the inner layer and the diffuse layer, respectively. The solution of the Poisson−Boltzmann theory gives $C_{\text{diff}} \sim C^{1/2}$, where C is the concentration.

4. CONCLUSIONS

In concolusion, we have studied the capacitive properties of microtube bundle carbons and the influence of the macropore shape and structure on their electrochemical properties. MTBCs were prepared from carbonized biomass of PS which was activated at 800 °C under N_2 flow. Experimental results showed the resulting MTBCs presented high surface areas (about 1900 $m^2\ g^{-1}$) with an abundance of macropores as well as micropores and mesopores. Cyclic voltammetry, galvanostatic charge/discharge, and electrochemical impedance spectroscopy demonstrated the excellent charge storage, transfer capability, and low impedance of MTBCs. The specific capacitance of MTBCs-3 and MTBCs-4 was 201 and 227 F g^{-1} at 2 mV s^{-1} and 92 and 71 F g^{-1} at 100 mV s^{-1}, respectively. Moreover, the electrostatic capacitor performance was found in the electrochemical impedance spectroscopy. On the basis of the experimental results, a model of the schematic of MTBC supercapacitors was also proposed. It could explain those interesting phenomena that MTBCs-3 showed the highest capacitance as compared with others at high scan rate and electrostatic capacitors that existed at low frequency current. Macropores are important for providing a smooth charge-transfer pathway for the ions in electrolytes and gateways to micropores and mesopores in the bulk. The model of electrical double-layer supercapacitors of carbon microtubes provided the pathways for easy accessibility of efficient charge transport and enhanced the rate. These MTBCs showed a large reversible capacity and energy storage. Therefore, MTBCs may be a potential way to develop ideal supercapacitor devices and may be utilized as hybrid supercapacitors based on electrical double-layer capacitors and electrostatic capacitors.

AUTHOR INFORMATION

Corresponding Author

*E-mail: tliuyl@163.com.

Notes

The authors declare no competing financial interest.

ACKNOWLEDGMENTS

This work was supported by the National Natural Science Foundation of China (Nos. 21031001, U0734005, and 21201065), the Guangdong Higher Education Technology Innovation Key Project (cxzd1014), and the Science and Technology Plan Projects of Guangdong Province (2011A081301018).

REFERENCES

(1) Simon, P.; Gogotsi, Y. *Nat. Mater.* **2008**, *7*, 845−854.
(2) Miller, J. R.; Simon, P. *Science* **2008**, *321*, 651−652.
(3) Simon, P.; Gogotsi, Y. *Philos. Trans. R. Soc., A* **2010**, *368*, 3457−3467.
(4) Zhang, Y.; Feng, H.; Wu, X. B.; Wang, L. Z.; Zhang, A. Q.; Xu, T. C.; Dong, H. C.; Li, X. F.; Zhang, L. S. *Int. J. Hydrogen Energy* **2009**, *34*, 4889−4899.
(5) Wang, G. P.; Zhang, L.; Zhang, J. J. *Chem. Soc. Rev.* **2012**, *41*, 797−828.
(6) Michio, I.; Hidetaka, K.; Osamu, T. *J. Power Sources* **2010**, *195*, 7880−7903.
(7) Zhu, Y. W.; Murali, S.; Stoller, M. D.; Ganesh, K. J.; Cai, W. W.; Ferreira, P. J.; Pirkle, A.; Wallace, R. M.; Cychosz, K. A.; Thommes, M.; Su, D.; Stach, E. A.; Ruoff, R. S. *Science* **2011**, *332*, 1537−1541.
(8) Bueke, A. *Electrochim. Acta* **2007**, *53*, 1083−1091.
(9) Izadi-Najiafabadi, A.; Yasuda, S.; Kobashi, K. *Adv. Mater.* **2010**, *22*, E235−E241.
(10) Izadi-Najafabadi, A.; Takeo, Y.; Futaba, D. N.; Yudasaka, M.; Takagi, H.; Hatori, H.; Sumio, L.; Hata, K. *ACS Nano* **2011**, *5*, 811−819.
(11) Zhang, L. L.; Zhao, X. S. *Chem. Soc. Rev.* **2009**, *38*, 2520−2531.
(12) Dai, L. M.; Chang, D. W.; Jong-Beom, B.; Lu, W. *Small* **2012**, *8*, 1130−1166.
(13) Ghosh, A.; Lee, Y. H. *ChemSusChem* **2012**, *5*, 480−499.
(14) Liu, H. J.; Wang, X. M.; Cui, W. J.; Dou, Y. Q.; Zhao, D. Y.; Xia, Y. Y. *J. Mater. Chem.* **2010**, *20*, 4223−4230.
(15) Ruan, G. D.; Sun, Z. Z.; Peng, Z. W.; Tour, J. M. *ACS Nano* **2011**, *5*, 7601−7607.
(16) Chen, H. B.; Wang, H. B.; Yang, L. F.; Xiao, Y.; Zheng, M. T.; Liu, Y. L.; Fu, H. G. *Int. J. Electrochem. Sci.* **2012**, *7*, 4889−4897.
(17) Lv, Y. K.; Gan, L. H.; Liu, M. X.; Xiong, W.; Xu, Z. J.; Zhu, D. Z.; Wright, D. S. *J. Power Sources* **2012**, *209*, 152−157.
(18) Elmouwahidi, A.; Zapata-Benabithe, Z.; Carrasco-Marín, F.; Moreno-Castilla, C. *Bioresour. Technol.* **2012**, *111*, 185−190.
(19) Ashori, A.; Nourbakhsh, A. *Eur. J. Wood Wood Prod.* **2009**, *67*, 323−327.
(20) Brunauer, S.; Emmett, P. H.; Teller, E. *J. Am. Chem. Soc.* **1938**, *60*, 309−319.
(21) Chen, L. F.; Zhang, X. D.; Liang, H. W.; Kong, M. G.; Guan, Q. F.; Chen, P.; Wu, Z. Y.; Yu, S. H. *ACS Nano* **2012**, *6*, 7092−7102.
(22) Lillo-Ródenas, M. A.; Cazorla-Amorós, D.; Linares-Solano, A. *Carbon* **2003**, *41*, 267−275.
(23) Cazetta, A. L.; Vargas, A. M.; Nogami, E. M.; Kunita, M. H.; Guilherme, M. R.; Martins, A. C.; Silva, T. L.; Moraaes, J. C. G.; Almeida, V. C. *Chem. Eng. J.* **2011**, *174*, 117−125.
(24) Tashima, D.; Yamamoto, E.; Kai, N.; Fujikawa, D.; Sakai, G.; Kijima, T. *Carbon* **2011**, *49*, 848−857.
(25) Nguyen, C. H.; Anoshkin, I. V.; Rakov, E. G. *Russ. J. Appl. Chem.* **2007**, *80*, 443−447.
(26) Ravikovitch, P. I.; Vishnyakov, A.; Russo, R. *Langmuir* **2000**, *16*, 2311−2320.
(27) Hang, S. *Electrochim. Acta* **1996**, *41*, 1633−1639.
(28) Chmiola, J.; Yushin, G.; Dash, R.; Gogotsi, Y. *J. Power Sources* **2006**, *158*, 765−772.
(29) Hu, C. C.; Tsou, T. W. *J. Power Sources* **2003**, *115*, 179−186.
(30) Conway, B. E. *Electrochemical Supercapacitors: Scientific Fundamentals and Technological Applications*; Conway, B. E., Ed.; Kluwer Academic/Plenum Publishers: New York, 1999.
(31) Zhang, H.; Cao, G. P.; Wang, Z. Y.; Yang, Y. S.; Shi, Z. J.; Gu, Z. N. *Electrochem. Commun.* **2008**, *10*, 1056−1059.
(32) Fang, Y. X.; Guo, S. J.; Li, D.; Zhu, C. Z.; Ren, W.; Dong, S. J.; Wang, E. K. *ACS Nano* **2012**, *6*, 400−409.
(33) Debra, R. R. *Science* **2003**, *299*, 1698−1701.
(34) Taberna, P. L.; Simon, P.; Fauvarque, J. F. *J. Electrochem. Soc.* **2003**, *150*, A292−A300.
(35) Wang, Y. G.; Li, H. Q.; Xia, Y. Y. *Adv. Mater.* **2006**, *18*, 2619−2623.

(36) Frank, M. W. *Fluid Mechanics*, 5th ed.; Frank, M. W., Ed.; McGraw Hill: New York, 2004; Chapter 10.
(37) Gouy, G. *J. Phys. (Paris)* **1910**, *9*, 457.
(38) Chapman, D. L. *Philos. Mag.* **1913**, *25*, 475−481.